Accepted Manuscript

Observation of enhanced magnetic pinning in Sm^{3+} substituted nanocrystalline Mn–Zn ferrites prepared by propellant chemistry route

V. Jagadeesha Angadi, A.V. Anupama, R. Kumar, S. Matteppanavar, B. Rudraswamy, B. Sahoo

PII: S0925-8388(16)31224-5

DOI: 10.1016/j.jallcom.2016.04.246

Reference: JALCOM 37444

To appear in: *Journal of Alloys and Compounds*

Received Date: 27 January 2016

Revised Date: 22 April 2016

Accepted Date: 23 April 2016

Please cite this article as: V. Jagadeesha Angadi, A.V. Anupama, R. Kumar, S. Matteppanavar, B. Rudraswamy, B. Sahoo, Observation of enhanced magnetic pinning in Sm^{3+} substituted nanocrystalline Mn–Zn ferrites prepared by propellant chemistry route, *Journal of Alloys and Compounds* (2016), doi: 10.1016/j.jallcom.2016.04.246.

$Mn_{0.5}Zn_{0.5}Fe_{2-y}Sm_yO_4$

Particle size and magnetic hysteresis loops

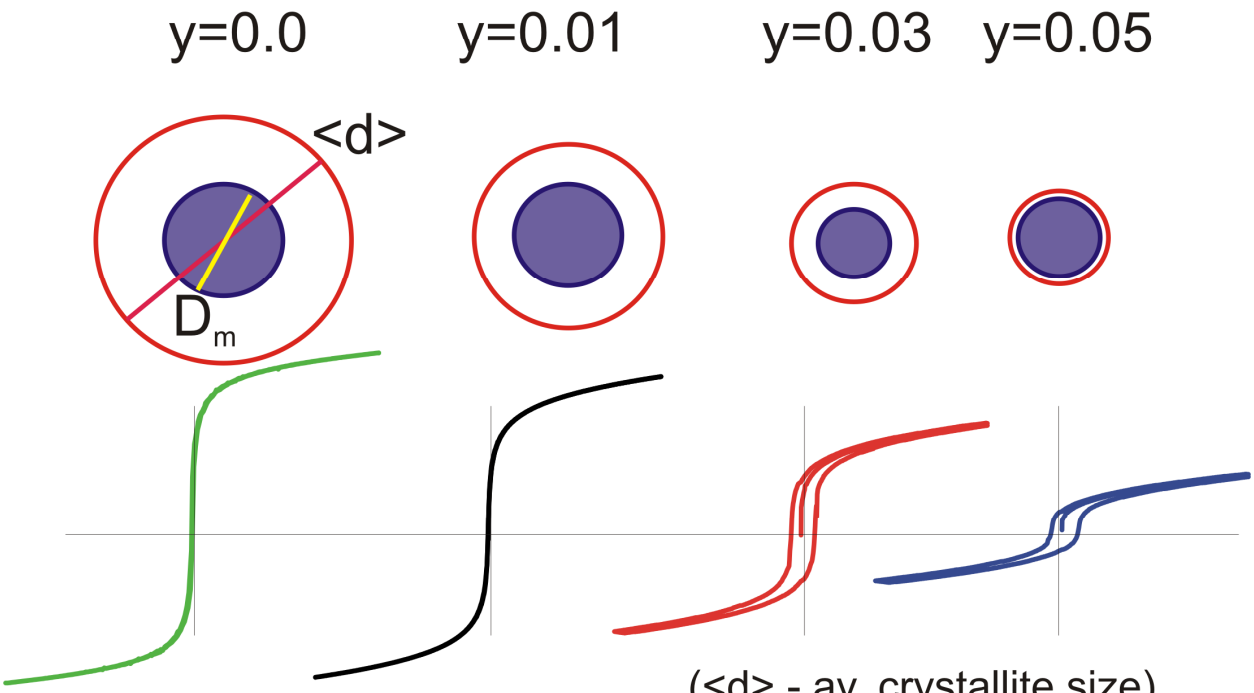

(<d> - av. crystallite size)
(D_m-magnetic particle size)

Observation of enhanced magnetic pinning in Sm^{3+} substituted nanocrystalline Mn-Zn ferrites prepared by propellant chemistry route

V. Jagadeesha Angadi [1], Anupama A.V. [2], R. Kumar[2], S. Matteppanavar[1], Rudraswamy B.[1] and B. Sahoo[2,*]

[1]Department of Physics, Bangalore University, Bangalore-560056, India

[2]Materials Research Centre, Indian Institute of Science, Bangalore-560012, India

**Corresponding author:*

email: bsahoo@mrc.iisc.ernet.in

Tel: +91-80-22932943

Abstract

We report the effect of Sm^{3+} substitution on the structural and magnetic properties of nanocrystalline $Mn_{0.5}Zn_{0.5}Sm_yFe_{2-y}O_4$ (y = 0.00, 0.01, 0.03 and 0.05) samples prepared by propellant chemistry route using a mixture of fuels. Rietveld refinement of XRD patterns confirmed the formation of cubic spinel phase with space group $\boldsymbol{Fd\bar{3}m}$. The lattice parameter values decreased with Sm^{3+} substitution up to y = 0.03, but with a noticeable increase for the sample with y = 0.05. In all the samples, entire amount of Zn^{2+} and Sm^{3+} were found to be present at the A and B sites, respectively. A distribution of Mn^{2+} ions at the tetrahedral (A) and the octahedral (B) sites of the spinel $Mn_{0.5}Zn_{0.5}Fe_2O_4$ was observed. The microstructure of the samples was observed using Scanning Electron Microscopy (SEM) and Transmission Electron Microscopy (TEM). For all the samples, the average crystallite size decreased with increase in Sm^{3+} concentration, as determined using Williamson-Hall method. The FTIR spectra showed prominent absorption bands at ~ 540 and ~ 390 cm^{-1} corresponding to the stretching vibrations of the metal ion complexes at the tetrahedral (A) and the octahedral (B) sites, respectively. Magnetic properties such as saturation magnetization (M_s), remanence (M_r) and magneton number (η_B) were found to decrease, while the coercivity (H_c) and reduced remanence (M_r/M_s) of the samples were found to increase with increasing Sm^{3+} content. The increase in H_c with increase in Sm^{3+} concentration is interpreted as the enhanced pinning of the magnetic moments at the magnetic defects created by Sm^{3+} ions, which is further confirmed by Mössbauer spectroscopy through a nearly constant magnetic hyperfine field. This results in an increase in the magnetic particle size in spite of decreasing average crystallite size. Our work suggests that, Sm^{3+} substitution can be used to alter the magnetic hardness of Mn-Zn ferrites and to enable them to be used as potential materials for various technological applications.

Keywords: Mn-Zn ferrites, Magnetic pinning, Yafet-Kittel angle, Mössbauer spectroscopy, Rietveld refinement

1. INTRODUCTION

Mn-Zn nano-ferrites possess excellent magnetic and electric properties, in particular, high permeability, high saturation magnetization, high resistivity and low power loss [1-4]. A lot of emphasis has been given to study the properties of rare earth ion substituted Mn-Zn ferrites as potential candidates for use in magneto-optical devices that require high saturation magnetization, high coercivity and high anisotropy constant [5]. In particular, the substitution of Sm^{3+} ions at the Fe^{3+} site are known to produce very interesting physical and chemical properties in spinel ferrites [6-11]. In view of the wide potential for technological applications such as, wide band microwave absorption [12], magneto-acoustics [13], magneto-caloric pumping [14, 15], temperature sensitive ferrofluids [16], heat-exchange devices [17, 18] and rare-earth doped Mn-Zn ferrite pyromagnetic applications [19, 20], the Sm-substituted Mn-Zn ferrites are chosen in the present study. Furthermore, rare earth ion substituted ferrites can be synthesized by several methods such as solid state reaction route [12], chemical co-precipitation method [21-23], hydrothermal method [24, 25], sol-gel synthesis [26, 27], spray pyrolysis [28] and citrate precursor method [29]. However, most of these methods are economically infeasible for large scale production of ferrites. The solution combustion method, also known as propellant chemistry method, is advantageous due to its simplicity, short reaction time and inexpensiveness. Unlike solid state synthesis route, this method can produce fine, homogeneous crystalline powder with an added advantage of lower consumption of energy and elimination of intermediate calcination stages during synthesis [30]. Therefore, in the present investigation we have adopted propellant chemistry route [31] to obtain nanosized Sm-substituted Mn-Zn ferrite nano-particles.

A detailed investigation on the influence of Sm^{3+}substitution on structural and magnetic properties of $Mn_{0.5}Zn_{0.5}Sm_yFe_{2-y}O_4$ (y = 0.00, 0.01, 0.03 and 0.05) samples is taken up.

2. EXPERIMENT

2.1 Synthesis method

Nanocrystalline $Mn_{0.5}Zn_{0.5}Sm_yFe_{2-y}O_4$ (y = 0.00, 0.01, 0.03 and 0.05) samples were synthesized by propellant chemistry route using stoichiometric amounts of the following oxidizers (precursors): manganese nitrate [$Mn(NO_3)_2 \cdot 4H_2O$], zinc nitrate [$Zn(NO_3)_2 \cdot 6H_2O$], iron nitrate [$Fe(NO_3)_3 \cdot 9H_2O$] and samarium nitrate [$Sm(NO_3)_3 \cdot 9H_2O$]. For the preparation of each sample, a constant molar concentration (1.1139 mM) was prepared by dissolving 15 mg of $Fe(NO_3)_3 \cdot 9H_2O$ in 30 ml of double distilled water. Stoichiometric proportions of $Mn(NO_3)_2 \cdot 4H_2O$, $Zn(NO_3)_2 \cdot 6H_2O$ and $Sm(NO_3)_3 \cdot 9H_2O$ were then added to this solution. A mixture of urea [NH_2CONH_2] and glucose [$C_6H_{12}O_6$)] in the ratio 3:2 was taken as fuel. An equimolar ratio of oxidizers to fuel was taken based on the oxidizing and reducing valencies of the compounds [31]. The mixture of fuels is taken for increased exothermicity and completion of the reaction, which can be understood on the basis of chemical reactions involved during the process [32]. The metal nitrates and fuels were dissolved by using a magnetic stirrer for one hour, until the formation of homogenous solution. This homogeneous solution was taken in a Pyrex dish and kept in a pre-heated muffle furnace maintained at 450 ± 10 °C. Initially, the solution boiled and subsequently frothed to yield fine powder. The combustion process completed within 20 min. The obtained samples were then ground properly and characterized.

2.2 Characterizations

2.2.1 X-ray diffraction and Rietveld refinement

The $Mn_{0.5}Zn_{0.5}Fe_{2-y}Sm_yO_4$ samples with y = 0, 0.01, 0.03 and 0.05 were characterized by powder X-ray diffraction using “PANalytical X’Pert Pro MPD” diffractometer (Cu-K_α radiation, Ni filter). The diffraction data (Fig. 1(a)) were recorded in the detector angle (2θ) range of 10-

80° with a step size of 0.02°. The crystalline phases in the samples were identified by referring to the Bragg positions and their relative intensities. The structural and compositional details of the phases in each sample were extracted by the Rietveld refinement of the respective XRD data. The Rietveld refinement was performed using the program "FullProf" [33]. The information required for the starting model for the refinement such as crystal structure, atomic co-ordinates and initial cell parameters were taken from crystallographic information files (CIF) from *Inorganic Crystal Structure Database* (ICSD). Instrumental error corrections were considered during the least square fitting of the XRD pattern. For refinement, Thomson-Cox-Hastings profile was adopted. The lattice parameters, scale factor, full width at half maximum (FWHM) of the Bragg reflections were refined. The quality of fit to the observed XRD patterns were assessed by the Rietveld agreement (reliability) factors: R-pattern factor (R_p), R-weighted pattern factor (R_{wp}), R-expected (R_{exp}) and χ^2 [34]. The refined lattice parameters and occupancy factors of cations in the cubic spinel interstitials were obtained. The crystallite size and lattice strain were estimated using Williamson-Hall method [35]. The Rietveld refined XRD patterns are shown in Fig. 1. The refined parameters and the agreement factors are given in Table I and the cation occupancies are listed in Table II.

2.2.2 Electron Microscopy

Fig. 4 shows the SEM images of the analyzed samples taken using "Ultra 55 Scanning Electron Microscope" with electron energy of 5 kV. The TEM images (Fig. 5) were taken by FETEM with electron energy of 200 kV. The particles sizes were measured using "ImageJ" software. To obtain a size distribution histogram (Fig. 5) a minimum of 50 particles were taken into account. The obtained average particle sizes are listed in Table I.

2.2.3 Mössbauer spectroscopy

All the synthesized samples (i.e., y = 0.0, 0.01, 0.03 and 0.05) were characterized by Mössbauer spectroscopy at room temperature (RT) in transmission geometry by using a

constant-acceleration Doppler velocity drive with ^{57}Co-source (Rh-matrix). The spectra were recorded by using a proportional counter. The velocity of Mössbauer drive was calibrated using α-Fe foil at RT, which gives an isomer shift of -0.106 mm/s relative to the ^{57}Co-source (Rh-matrix). The spectra obtained were least square fit using "NORMOS" program [36, 37]. The spectra after the least square fit are shown in Fig. 6. Mössbauer spectral parameters such as isomer shift (***IS***), quadrupole splitting (***QS***), magnetic hyperfine field ($\boldsymbol{B_{hf}}$) and spectral area were obtained and tabulated in Table III. All the isomer shifts are given with respect to the ^{57}Co-source (Rh-matrix). The distribution profiles of the magnetic hyperfine field parameters ($\boldsymbol{B_{hf}}$) are plotted beside each Mössbauer spectrum.

2.2.4 FTIR spectroscopy

The FTIR spectroscopy is an important tool to probe various structural ordering phenomena, and this technique provides the information about the position of ions in the crystal and about the interatomic vibration modes [38]. The stretching and bending vibrations of bonded atoms, molecules or functional groups in the samples could be probed which gives important insights into structural and compositional order present in the samples. The absorption of specific wavelength IR radiation depends on the natural frequency of vibration of the functional group/moiety. The position and appearance of the absorption bands depend on the bond length, bond strength, and the mass/size of the atoms or molecules involved. The FTIR spectra for our samples (y = 0.0, 0.01, 0.03 and 0.05) were recorded in the wave number range 350-4000 cm^{-1} using "Agilent" FTIR spectrometer and are shown in Fig. 7.

2.2.5 Vibrating sample magnetometry

The room temperature magnetization measurements were carried out by "PPMS-14T" vibrating sample magnetometer (VSM). The value of reduced remanence $\boldsymbol{S}$ (= $\boldsymbol{M_r/M_s}$),

anisotropy constant (***K***), magneton number ($\boldsymbol{\eta_B}$), Yafet-Kittel angle ($\boldsymbol{\alpha_{Y\text{-}K}}$) and magnetic particle size ($\boldsymbol{D_m}$) were calculated using the equations (1), (2a, 2b), (3), (4) and (5), respectively [39].

Reduced remanence, a measure of the squareness of the hysteresis loop, is defined as:

$$S = \frac{M_r}{M_S} \quad (1),$$

where, $\boldsymbol{M_r}$ and $\boldsymbol{M_s}$ are the remanent and saturation magnetizations, respectively. According to the Stoner-Wohlfarth model for non-interacting 3D-random ferromagnetic particles, the reduced remanence is given by $\boldsymbol{S}$ = 0.5 for uniaxial anisotropy, and $\boldsymbol{S}$ = 0.832 for cubic anisotropy [40]. Furthermore, the anisotropy constant in these particles is related to the coercive field ($\boldsymbol{H_c}$) and the saturation magnetization ($\boldsymbol{M_s}$) according to the following relations.

The anisotropy constant (***K***) for the non-interacting ferrimagnetic particles

with uniaxial anisotropy $K_u = \frac{H_c \times M_s}{0.985}$ (2a),

and, with cubic anisotropy $K_c = \frac{H_c \times M_s}{0.64}$ (2b),

The value of $\boldsymbol{H_c}$ is calculated by measuring $\boldsymbol{-H_c}$ to $\boldsymbol{+H_c}$ and averaging the value.

Magneton number ($\boldsymbol{\eta_B}$) is the magnetic moment of a ferrimagnetic material in units of Bohr magneton ($\boldsymbol{\mu_B}$). The magneton numbers for our samples were calculated using the formula below.

Magneton number: $\eta_B = \frac{M_W \times M_S}{N_A \times \mu_B}$ (3),

where, $\boldsymbol{M_W}$ is molecular weight of the compound in g, $\boldsymbol{M_s}$ is the saturation magnetization in emu/g, $\boldsymbol{N_A}$ is the Avogadro number and $\boldsymbol{\mu_B}$ is value of one Bohr magneton in emu.

As in our samples, the tetrahedral site is occupied by non-magnetic Zn^{2+} ions (see sec. 3.1), the Néel's two sub-lattice model of ferrimagnetism cannot be used. The effective super-exchange

interaction will make a triangular (canted) spin arrangement at the B-site. We have used the following formula [40, 41] to calculate the Yafet-Kittel (spin-canting) angle.

$$\text{Yafet-Kittel angle: } \cos\alpha_{Y-K} = \frac{\eta_B + M_A}{M_B} \quad (4),$$

where, $\boldsymbol{M_A}$ and $\boldsymbol{M_B}$ are the effective magnetic moments of tetrahedral (A) and octahedral (B) site-ions, respectively (see Table II).

Since our ferrimagnetic particles behave super-paramagnetically, we have used the following formula to estimate the magnetic particle size.

$$\text{Magnetic particle size: } \quad D_m = \sqrt[3]{\frac{18k_BT\chi_i}{\pi\rho(M_S)^2}} \quad (5),$$

where, the values of the initial magnetic susceptibility, $\boldsymbol{\chi_i} = (\boldsymbol{dM}/\boldsymbol{dH})_{\boldsymbol{H}\to 0}$, for each sample was calculated by the initial straight line region in the slope of the ***M*-*H*** loop, $\boldsymbol{k_B}$ is Boltzmann constant, ***T*** is the experimental temperature in absolute scale and $\boldsymbol{\rho}$ is the density obtained from the Rietveld refinement (X-ray density).

3. RESULTS AND DISCUSSION

3.1 Structure and Morphology

3.1.1 Rietveld refinement of XRD data

The Rietveld refinement performed on the XRD data of selected samples with Sm content y = 0, 0.01, 0.03 and 0.05, revealed that all the samples have single phase cubic spinel structure (space group $\boldsymbol{Fd\bar{3}m}$). The observed lattice parameter for the undoped sample $Mn_{0.5}Zn_{0.5}Fe_2O_4$ was 8.4344 Å. This value was significantly lower than the reported value of 8.4510 Å for bulk $Mn_{0.5}Zn_{0.5}Fe_2O_4$ [42].This shrinkage in lattice parameter can be attributed to two different factors: (a) change of lattice parameter and cation occupancy due to size effect (nano-size); (b) possible redistribution of cations in the octahedral and tetrahedral interstitial sites

[43, 44]. The average crystallite size and lattice strain calculated by using Williamson-Hall method (Table I) showed that the crystallites in our Mn-Zn ferrite sample were nanosized (~17.5nm). Hence, the observed lower lattice parameter for nanocrystalline Mn-Zn ferrites is in accordance with the literature values [43, 44]. Furthermore, we found that the undoped sample, $Mn_{0.5}Zn_{0.5}Fe_2O_4$, is a mixed cubic spinel. Refinement of cation occupancies showed that Zn^{2+} were found to be present only in the A site. Neutron diffraction studies [45], Mössbauer spectroscopy studies [46] and site-preference calculations [47] support our finding that Zn^{2+} ions with zero magnetic moment have a strong preference to occupy the tetrahedral (A) site. However, Mn^{2+} was found to be distributed over both interstitial sites with a preference to occupy the A site [48], while Fe^{3+} was mostly present in the B site, but a fraction occupying the A site was observed (Table II). The occupancy of smaller Fe^{3+} ion (radius: 63 pm) in tetrahedral site in place of bigger Mn^{2+} ions (radius: 80 pm) effectively reduces the lattice parameter.

For the Sm-substituted (y = 0.03 and 0.05) samples, the lattice parameters (Table I) showed an appreciably lower value when compared to the unsubstituted (y = 0.0) sample. The lattice parameter of the sample with y = 0.01 was comparable to the unsubstituted sample. The sample with y = 0.05 showed an appreciable increase in lattice parameter compared to the sample with y = 0.03. This observation can be explained by considering the occupancy of Sm^{3+} ions in the octahedral interstitials of the spinel. The Rietveld refinement of occupancies of Fe^{3+} and Sm^{3+} showed that Sm^{3+} ions occupy only the B site of the spinel, in all the samples. The refinement of occupancy of Zn^{2+} showed no significant changes from its preferred A-site occupancy. Due to the preferential occupancy of Sm^{3+} in the B site, there is rearrangement of (Mn^{2+} and Fe^{3+}) cations within the interstitials. The lattice parameter variation due to this rearrangement could be understood as follows. The variation in lattice parameter with Sm^{3+} substitution does not follow Vegard's law. Two competing factors are responsible for this behavior (i) the mismatch between the ionic radii of the cations and the size of interstitial sites;

and (ii) the charge (valency) differences between the cations. The tetrahedral site, being smaller (lower bond length and strong interaction), is sensitive to any small changes in the ionic sizes of the atoms positioned within the site. Octahedral site, on the other hand, is bigger and bond strength is lower, wherein the occupancy of ions of different ionic sizes will show up its effect progressively, e.g., with substitution of Sm^{3+} ions. From the Rietveld refinement results of cation occupancies, we have observed that substitution of Sm^{3+} ions (radius: 107.9 pm) [49, 50] in the B site resulted in a proportional displacement of Fe^{3+} ions (radius: 63 pm) [49, 50] to the tetrahedral (A) site, thereby, proportionally displacing Mn^{2+} ions (radius: 81 pm) [49, 50] to the octahedral (B) site. For smaller concentrations of the dopant (Sm^{3+}) (i.e., for samples with y = 0.01-0.03), the effect of difference in ionic sizes of cations and their valencies in A-site dominates, reducing the lattice parameter of the sample (as Fe^{3+} has smaller ionic radii compared to Mn^{2+}). However, for the sample with y = 0.05, we speculate that the presence of more Mn^{2+} and Sm^{3+} in B site, which have larger ionic sizes than Fe^{3+}, has more effect on the lattice parameter than the effect of increased number of Fe^{3+} in A-site. The lattice parameter variation with Sm^{3+} content in the sample is shown in Fig. 3 and tabulated in Table I. The maximum error in the estimation of lattice parameter can be in the fourth decimal value.

. The average crystallite size, evaluated by Williamson-Hall method, was found to decrease with Sm^{3+} content. The values of lattice strain were ranging between 0.9-1.0 $\times 10^{-3}$ with an increasing trend with Sm^{3+} content. We understood that the substitution of Sm^{3+} in B site might have resulted in increased lattice strain inhibiting the crystallite growth.

From the fit to each Bragg reflection in the Rietveld refined XRD pattern, it can be noticed that there exists an ill-fit to the upper regions of the peaks throughout the pattern (Fig. 1). This has repercussions resulting in high value of R-factors (agreement factors) listed in Table I. This misfit may be due to the existance of a wide particle size distribution. To estimate the minimum and maximum crystallite sizes in the sample, the most intense (311) peak, where this

ill-fit is more evident, was considered. The (311) peaks of individual patterns was fit by two pseudo-Voigt functions as shown in Fig. 2. The FWHM of each pseudo-Voigt plot was taken during the maximum and minimum average crystallite size estimation by Scherrer method. The obtained minimum and maximum average particle sizes are listed within the square brackets in Table I.

3.1.2 Electron Microscopy (SEM and TEM)

The SEM micrographs (Fig. 4) of the samples show highly porous structures. The structures seem to contain a lot of defects. The appearance of the dry foamy powder is due to the evolution of the gases during the combustion process. As the particle sizes could not be determined from these pictures, we have performed the TEM investigation. The TEM images (Fig. 5) reveal that the particle size decreases with Sm^{3+} doping. The results are consistent with the trend in variation of particle sizes obtained by Williamson-Hall method from the XRD data. However, the observed differences in the absolute values of the average particle sizes could be arising due to the volume occupied by the bigger particles within the experimental volume is large, although the number of such particles is small. This leads to the sharper lines in the XRD (bigger average particle size) but the average number of small particles is more (as seen by TEM).

3.2 Mössbauer spectroscopy

The Mössbauer spectra of all the $Mn_{0.5}Zn_{0.5}Fe_{2-y}Sm_yO_4$ samples with y = 0, 0.01, 0.03 and 0.05, recorded at RT are shown in Fig. 6. For the samples with y = 0.0-0.03, a Zeemann split broad (low intensity) sextet and a strong central doublet were seen. With increasing Sm-substitution, the sextet contribution seemed to disappear to an apparent doublet and for the sample with y = 0.05 only a central doublet was seen. The line width of the central doublet was seen to be high for y = 0.05. This behaviour was not expected for high Sm-content sample, as the sample may behave like more superparamagnetic. Hence, this change in line width of the central

doublet could not be explained only by a distribution of quadrupole doublets. Thus, the spectra corresponding to all samples were initially fit by distributions of sextets and doublets. Due to the limitation in assuming only a certain number of sub-spectra in the NORMOS program, the results showed majorly quadrupole split doublets which overestimate the paramagnetic behaviour for the Sm-substituted samples. Thus, only distributions of sextets were then considered for the least square fit of the observed Mössbauer spectra. However, the results were erroneous, because the isomer shifts corresponding to the sextet distribution and the central doublet are different. Considering the decrease in particle size with Sm content in the samples and that in view of a strong central doublet seen regardless of the composition of the sample with slight increase in width, a distribution of sextets along with a crystalline doublet were then considered as the fitting model for all the samples. During the least square fit to the observed Mössbauer spectra, the values of ***IS***, ***QS*** and line-width of the doublet for all samples were fixed to the approximate values of pure zinc ferrite (***IS*** = 0.235 mm/s, ***QS*** = 0.5 mm/s and line width = 0.45 mm/s) [51, 52]. The spectra after the fit are shown in Fig. 6 and resultant hyperfine parameters are listed in Table III.

From the Mössbauer spectrum of the undoped $Mn_{0.5}Zn_{0.5}Fe_2O_4$ (y = 0.0) sample, shown in Fig. 6(a), it is clear that there exists a Zeemann split broad sextet component along with a central doublet. Hence, the spectrum was fit by distribution of sextets and a doublet. We believe that the local compositional fluctuation leads to formation of Zn-ferrite like tiny regions in the sample, which results in the central doublet observed in the Mössbauer spectrum. The origin of the other sub-spectrum (the sextet distributions) could be due to: (i) the slow spin relaxation of the bigger particles from the wide distribution of particle sizes as discussed in section 3.1; and (ii) the partial substitution by Mn^{2+} ions in place of Fe^{3+} ions at the B-site in the spinel structure of $Mn_{0.5}Zn_{0.5}Fe_2O_4$. In the latter case, as observed by XRD results, Zn^{2+} occupies A site and Mn^{2+} is distributed among the available A and B sites, leading to a partial occupation of Fe^{3+} at

the A site. The resulting formula can be represented as $(Zn_{0.5}Mn_{0.5-x}Fe_x)[Mn_yFe_{2-y}]O_4$. Hence, the A-B ($Fe^{3+}$-$Fe^{3+}$) super-exchange interaction becomes stronger resulting in a broad sextet in the Mössbauer spectrum. The other exchange interaction which might provide magnetic ordering of Fe atoms is between Fe^{3+}-Mn^{2+} (A-B interaction). Thus, the magnetic hyperfine field distribution seen in Fig. 4(a) right, is due to the A-B site super-exchange interaction between Fe^{3+}-Fe^{3+} and Fe^{3+}-Mn^{2+}. We assign the larger $\boldsymbol{B_{hf}}$ (~ 35-50 T) to Fe^{3+}-Fe^{3+} interaction and smaller $\boldsymbol{B_{hf}}$ (~ 15-35 T) to Fe^{3+}-Mn^{2+} interaction. The $\boldsymbol{B_{hf}}$ values in the range 0-10 T, are due to the superparamagnetic relaxation of very small particles present in this sample.

The same fitting model (a sextet distribution and a doublet) was assumed for the least square fitting of all the Sm-doped samples. For these Sm-doped samples, as in the case of undoped Mn-Zn ferrite, the presence of Zn-ferrite-like local tiny regions result in the crystalline central doublet (DX1, where X = 1, 2, 3 and 4, in Table III). During least square fit of the Mössbauer spectra, the values of ***IS***, ***QS*** and spectral line widths for this doublet were fixed to 0.235 mm/s, 0.5 mm/s and 0.45 mm/s, respectively, (Table III) [51, 52]. For each sample, the rest of the spectrum was consistently fit by a distribution of sextets as given in Fig. 6. From the probability distribution, $\boldsymbol{P(B_{hf})}$, (area under the Zeemann split sextet distribution, Fig. 6 and Table III), it can be observed that the average value of $\boldsymbol{B_{hf}}$ ($\boldsymbol{<B_{hf}>}$) decreases with increase in Sm content in the samples. For the sample with y = 0.01 (Fig. 6(b)), the spectrum fit by distribution of sextets and a single doublet, in a manner similar to that of $Mn_{0.5}Zn_{0.5}Fe_2O_4$ (y = 0.0) sample, showed that the intensity of the sextet distribution decreases by Sm-doping. The peak values of $\boldsymbol{P(B_{hf})}$ (Table III) are assigned to the magnetic ordering due to Fe^{3+}-Fe^{3+}, Fe^{3+}-Mn^{2+} and Fe^{3+}-Sm^{3+} interactions, respectively. The observed value of $\boldsymbol{<B_{hf}>}$ was found to decrease as compared to the undoped sample, which is attributed to the reduced interaction strength due to incorporation of Sm^{3+} as Fe^{3+}-Sm^{3+} interaction is weak. The presence of Sm^{3+} between Fe^{3+} ions also reduces the super-exchange interaction between Fe^{3+}-Fe^{3+}.

For the sample with y = 0.03, the reduced magnetic ordering (area under the sextet distribution in Fig. 6(c)) resulted in further decrease of $\langle B_{hf} \rangle$ value, due to the increased Fe^{3+}-Sm^{3+} interactions. There were no peaks observed in the B_{hf} distribution corresponding to Fe^{3+}-Fe^{3+} and Fe^{3+}-Mn^{2+} interactions. The sample with y = 0.05, showed no clear Zeemann split sextet pattern as the exchange interaction between Fe^{3+}-Sm^{3+} dominated and the observed B_{hf} values were low. Interestingly, for the sample with y = 0.05, the $\langle B_{hf} \rangle$ value is nearly constant to that observed for the sample with y = 0.03. This, we believe, is due to the increased pinning of the Fe-moments. This aspect is explained further in section 3.4. For the Sm-substituted samples (with y = 0.01 and 0.03), the progressively narrower sextet distributions, which appear as doublets in the Mössbauer spectra, signify the superparamagnetic nature of small particles in the samples. The samples with y = 0.05 showed only superparamagnetic contribution due to very small crystallites (~ 3-13 nm) which is confirmed by XRD and TEM results (Table I). Surprisingly, the width of the sextet distribution which appears as a doublet was found to increase for sample y = 0.05 in comparison to the sample with y = 0.03. Simultaneously, the rate of decrease of the spectral area under the doublet considerably reduced (Table III). The origin of this behavior is explained as follows. It is well known that introduction of Sm^{3+} results in hard magnetic property [53], although there are reports on reduced magnetic anisotropy. The magnetic anisotropy enhancement/reduction due to Sm^{3+} doping depends on the type and position of other cations in the lattice. For all the samples, we have observed the enhancement of magnetic anisotropy [11] with increasing Sm concentration in vibrating sample magnetometry studies (see section 3.4). Thus, we attribute the broadening of the central doublet with Sm concentration to the enhancement of hard magnetic behaviour due to the pinning of magnetic moments in the sample which appears as a re-entrant magnetic ordering.

To emphasize, a superparamagnetic doublet was observed in addition to a (fixed width) crystalline quadrupole doublet in the Mössbauer spectra of all samples (Fig. 6 and Table III). The

average magnetic hyperfine field $<B_{hf}>$ was seen to decrease with increasing Sm-content, suggesting the increase in superparamagnetic behaviour of the nanoparticles. However, for the sample with y = 0.03 and 0.05, the nearly constant $<B_{hf}>$ (Table III) is due to the enhancement in the pinning of the Fe-spins at the 'defect' created in the bulk of the nanoparticles in the sample with y = 0.05. The crystalline doublet is assigned to the paramagnetic property of zinc ferrite ($ZnFe_2O_4$) type-local atomic ordering in the samples. The compositional disorder in the samples might have been produced due to local disorder in the arrangement of Mn^{2+}, Zn^{2+} and Fe^{3+} ions in the available tetrahedral and octahedral sites.

3.3 FTIR Spectroscopy

Infrared spectra of all the samples (Fig. 7) showed two prominent absorption bands, one (ν_1) at ~540 cm^{-1} attributed to the stretching vibration of tetrahedral complexes and the other (ν_2) at ~390 cm^{-1} assigned to the vibration of octahedral complexes. The difference in frequencies between ν_1 and ν_2 is due to the changes in co-ordination number and bond length (Fe^{3+}-O^{2-}) at tetrahedral and octahedral sites [38, 54]. The slight variation in band intensity from sample to sample may be related to the sample preparation conditions (for the FTIR measurement) and also to the particle size distribution (Fig. 2, 5). The band position ν_1 was almost invariant with respect to Sm^{3+} substitution. This supports the XRD result that Sm^{3+} ions occupy the octahedral (B) sites [55]. It can be seen that the absorption band ν_1 does not show any splitting (shoulders) and hence, the possibility of Fe^{2+} ions at the A-sites is ruled out [54]. On increasing the substitution of the Sm^{3+} ions, ν_2 should shift slightly towards lower frequency side due to the larger atomic mass and volume of the (Sm^{3+}) dopant in comparison to the (Fe^{3+}) host, which affects the effective reduced mass on octahedral sites, and hence, the band position. However, due to the limitations of our FTIR spectrometer in observing absorption bands below 400 cm^{-1}, the spectra

are noisy and no conclusive evidence regarding the occupancy of Sm^{3+} at the octahedral site was obtained.

The peaks observed at ~1300-1700 cm^{-1} are due to the presence of after combustion carbonaceous residue. The peaks around 2380 cm^{-1} and ~3300 cm^{-1} are attributed to the atmospheric CO_2 and -OH stretching vibrations (moisture), respectively.

3.4 Magnetic properties

Fig. 8 shows the magnetic hysteresis loops for the samples measured at room temperature with a maximum applied magnetic field of 20 kOe. It is clear that the saturation magnetization ($\boldsymbol{M_s}$) decreased with increasing Sm-doping. The $\boldsymbol{M_s}$ values of all the samples were obtained as follows: a straight line was extrapolated from the linear region of magnetization curve (i.e., from the high applied magnetic field region, which corresponds to near saturation magnetization of the sample) towards the magnetization axis. The intercept of this line with the magnetization axis was taken as the saturation magnetization $\boldsymbol{M_s}$. The $\boldsymbol{M_s}$ values of all the samples are listed in Table IV. For the undoped $Mn_{0.5}Zn_{0.5}Fe_2O_4$ sample, a lower value of $\boldsymbol{M_s}$ as compared to bulk was obtained along with a very narrow 'S-shaped' hysteresis loop, which suggests the presence of superparamagnetic and single-domain particles. For the Sm-substituted samples, the values of $\boldsymbol{M_s}$ were found to decrease further with increase in Sm-content. This decrease in $\boldsymbol{M_s}$ values might be related to the decrease in size of the nanoparticles as observed from the XRD and TEM results (Table I). This decrease in $\boldsymbol{M_s}$ might also be because, the substituted Sm^{3+} ions have the magnetic moment of 1.58 $\boldsymbol{\mu_B}$ ($\boldsymbol{\eta_B}$ = 1.58) [56, 57] which is less than that of Fe^{3+} ($\boldsymbol{\eta_B} = 5\boldsymbol{\mu_B}$) and Mn^{2+} ($\boldsymbol{\eta_B} = 2\boldsymbol{\mu_B}$), at room temperature [56, 58]. Furthermore, the 4f electrons of Sm^{3+} do not have strong exchange interaction with the 3d electrons of Fe^{3+}. Hence, the magnetic dipoles (magnetic moments) of Sm^{3+} ions, originating from the 4f electrons, are randomly oriented at room temperature. They are isolated (not strongly interacting with other atoms) and behave as "paramagnetic-like-defect" atoms occupying the B site. This results in a much weaker Mn^{2+}-

Sm^{3+} (A-B) interaction as compared to the stronger Mn^{2+}-Fe^{3+} super-exchange interaction. It can be noticed from Fig. 8 that for higher Sm^{3+} doping ($y \geq 0.03$), the increasing field branch of the hysteresis loop does not merge with the decreasing field branch. This is a clear indication of the magnetic anisotropy (spin orbit coupling of *3d*- and *4f*-electrons) introduced due to the Sm^{3+} doping.

The remanent magnetization ($\boldsymbol{M_r}$) values extracted by the intercept of ***M*-*H*** loop on the magnetization axis are listed in Table III. It can be observed that the $\boldsymbol{M_r}$ values were not varying monotonically with Sm-content in the samples. The $\boldsymbol{M_r}$ value for the sample with y = 0.01 was the lowest, which suggests that a slight doping of the Sm^{3+} ions the sample shows "higher" superparamagnetic-like behaviour. Higher superparamagnetic behaviour means that the particle-particle interaction becomes negligible. This is also evidenced from the comparison between the Mössbauer spectra of the undoped $Mn_{0.5}Zn_{0.5}Fe_2O_4$ sample (Fig. 6(a)) with the Sm-doped (y = 0.01) sample (Fig. 6(b)). Here, the area under the broad Zeeman split sextet in Fig. 8(a) decreases dramatically and it gives rise to the superparamagnetic-doublet-like spectrum in Fig. 6(b). Quantitatively, the average magnetic hyperfine field $\langle \boldsymbol{B_{hf}} \rangle$ decreases from 24.3 T to 13.0 T (Table III). It was surprising to observe that the $\boldsymbol{M_r}$ values of the other samples (y = 0.03 and 0.05) are higher, although the saturation magnetization decreases with increasing Sm-content (y). Simultaneously, the Mössbauer spectra showed progressive increase in area under the "superparamagnetic-doublet" at the expense of the Zeeman split sextet. Note that this effect is combined with the decrease in particle size and also saturation magnetization.

To understand this aspect better, we considered the quantity "reduced remanence ($\boldsymbol{S}$)" which is the ratio between $\boldsymbol{M_r}$ and $\boldsymbol{M_s}$ values (Eq. 1) of respective samples. Interestingly, as anticipated, the value of the reduced remanence was found to be the lowest for y = 0.01 sample and it is higher for higher Sm-doping. However, as observed from Mössbauer spectroscopy, all the samples are superparamagnetic in the Mössbauer spectroscopy time scale of 10^{-8} s. Had the

observed ***S*** values originated only from the higher superparamagnetism (due to decreased particle size and reduced particle-particle interaction), we would have observed a monotonic decrease in ***S***. Hence, we expect that the observed effect is dominated by the surface pinning and the change in intrinsic magnetic anisotropy of the particles due to Sm-doping.

According to Stoner-Wohlfarth model, the reduced remanence (***S***) of an assembly of non-interacting magnetic particles is given by 0.5 for samples with uniaxial anisotropy and 0.832 for samples with cubic anisotropy [39]. In our samples, the observed values of ***S*** for the samples with $y \leq 0.01$ are below 0.5 (Table IV), but for the samples with $y \geq 0.03$, are between 0.5 and 0.7. This suggests that the samples with $y \leq 0.01$ contain bigger non-interacting single domain particles which display uniaxial anisotropy and samples with $y \geq 0.03$ largely contain single domain particles that are not interacting and the observed anisotropy is of the cubic anisotropy type. It is interesting to note that there is a transition from uniaxial anisotropy to cubic anisotropy by doping higher amount of Sm^{3+} at the B-site of Mn-Zn ferrite. As the particle size goes on increasing one should expect to observe an increase in superparamagnetic nature and decrease in the ***S*** value. We believe that the observed transition is related to the magnetic anisotropy developed due to Sm-doping. Hence, we have taken Eq. 2(a, b) in the calculation of anisotropy constants ($\boldsymbol{K_c}$ and $\boldsymbol{K_u}$).

Furthermore, in particulate systems, the coercive field ($\boldsymbol{H_c}$) can be originated due to two reasons: (i) inter-particle interactions, and (ii) intra-particle interactions. The intra-particle interactions can be due to surface pinning and bulk magnetocrystalline anisotropy (spin-orbit interaction). From the values of ***S*** in our samples, the shape of the hysteresis loops and the Mössbauer spectra, it can be inferred that there exist both inter-and intra-particle interaction. The sample with y = 0.0 exhibits very narrow hysteresis loop revealing the soft magnetic behaviour with very weak inter-particle interaction. We expect that these inter-particle interactions for the Sm-doped samples are very weak too and that gradually decrease with increasing Sm-doping and

it can be neglected for higher Sm-doped samples. However, in the hysteresis loops of the Sm-doped samples, the coercive field values are found to increase with increasing Sm^{3+}concentration (Table IV) for $y \geq 0.03$, although the particle sizes were found to decrease monotonically (section 3.1). Hence, we expect that the observed behavior is due to pinning of the magnetization at the surfaces of the particles and at the higher amount of magnetic-defects created by increase in Sm-content.

The variation of $\boldsymbol{H_c}$ with particle size can be explained on the basis of domain structure and magnetic anisotropy of the crystallites. The particle size reduction with increasing Sm^{3+} substitution as observed by XRD and TEM results, explains the superparamagnetic behavior present in the samples with increase in Sm content (Table I). With the decrease of particle size, the surface to volume ratio increases and surface effect may induce a spin disorder in the surface layer that causes the spin-pinning to increase with decreasing particle size and in turn, with increase of Sm^{3+} content. However, it seems that for small amount of Sm-doping ($y \leq 0.01$), the superparamagnetic effect (decreased particle-particle interaction), is enhanced. As the Sm-content increased, the spins within the particles were more strongly pinned than the negligibly weak particle-particle interaction, which enhances $\boldsymbol{H_c}$. The particle-particle interaction is shielded by the pinning due to surface defects.

In our samples, the expected contribution to $\boldsymbol{H_c}$ due to intra-particle interaction is high. As discussed earlier, the contribution to $\boldsymbol{H_c}$ from surface pinning effects and from magneto-crystalline anisotropy is enhanced due to the Sm^{3+} doping. The observed increase in $\boldsymbol{H_c}$ of the higher Sm-doped samples ($y \geq 0.03$) based on magnetocrystalline anisotropy can be understood as below. The magneto-crystalline anisotropy energy associated with an assembly of nanosized particles sample can be estimated from the equation: $\boldsymbol{E_A = KVsin^2\theta}$, where, $\boldsymbol{K}$ is the anisotropy energy constant, $\boldsymbol{V}$ is the volume of the particles, and $\boldsymbol{\theta}$ is the angle between the magnetization and easy axis direction. With the increasing magnetic anisotropy, the height of the magnetic

anisotropy barrier (E_A) increases which requires higher external magnetic field for spin reversal. In pure Mn-ferrite, the magneto crystalline anisotropy is due to the presence of Mn^{2+} ions at the tetrahedral (A) sites of the spinel structure. As we replace Zn^{2+} at the Mn^{2+} site, the amount of Mn^{2+} at the A site decreases and effective magnetic anisotropy of the Mn-Zn ferrite decreases. Thus, the effective magnetic anisotropy and H_c are less for Mn-Zn ferrite, making it a very soft ferrite than pure Mn-ferrite. In the Sm-doped samples, the effective magnetic anisotropy is provided by the A-B exchange interaction between the Mn^{2+}-Fe^{3+}, Fe^{3+}-Fe^{3+}, Fe^{3+}-Mn^{2+}, Mn^{2+}-Sm^{3+} and Fe^{3+}-Sm^{3+}, and as discussed earlier, the domain wall pinning of the A-site and B-site Fe^{3+} and Mn^{2+} spins due to Sm^{3+} ion-substitution. The existence of random canting of particle surface spins, surface effects and the occurrence of a magnetic glassy state created by Sm-doping, can play an active role in reducing the saturation magnetization (M_s) values and enhancing the coercivity (H_c) values.

The magneton number (η_B) and the *Y-K* angle ($\alpha_{Y\text{-}K}$) were calculated using Eq. 3 and 4, and are listed in Table IV. The value of η_B strongly decreased with increase in the Sm-content, which suggests that the obtained M_s values cannot be explained by assuming Néel's two sub-lattice model for ferrimagnetism. According to Néel's two sub-lattice model of ferrimagnetism [59], the net magnetic moment per formula unit in ferrimagnetic ferrites is the resultant magnetic moment due to the antiferromagnetic ordering between tetrahedral (A) site and octahedral (B) site magnetic moments. The net magnetic moment is given by the difference between the A and B sub-lattice magnetic moments: $\eta_B = M_B(x) - M_A(x)$, where, M_A and M_B are the A and B sub-lattice magnetic moments in μ_B, respectively [40, 41]. However, in our undoped $Mn_{0.5}Zn_{0.5}Fe_2O_4$ sample, the presence of non-magnetic Zn^{2+} ions at the tetrahedral site invalidates the Néel's two sub-lattice model. We have used the triangular (three sub-lattice) spin arrangement model by Yafet and Kittel (Eq. 5) to calculate the so called Yafet-Kittel (Y-K) angle ($\alpha_{Y\text{-}K}$) in order to understand the degree of spin canting and the obtained M_s values [41]. Furthermore, as the

magnetic order of all the spinel ferrites result from the d-electron super-exchange interaction between the tetrahedral (A) and the octahedral (B) sites magnetic ions mediated by the oxygen ions, substituting Sm^{3+} ions, whose magnetization is due to f-electrons, the existing canted spin arrangement changes and the $\boldsymbol{\alpha_{Y\text{-}K}}$ alters. The calculated values of $\boldsymbol{\alpha_{Y\text{-}K}}$ (Table IV) are ranging between 70-80˚. This suggests the existence of canted (triangular) spin arrangement in all the samples (y = 0.0-0.05). The values of $\boldsymbol{\alpha_{Y\text{-}K}}$ of the sample with increasing Sm^{3+} concentration was found to increase. This increase in $\boldsymbol{\alpha_{Y\text{-}K}}$ and the presence of Zn^{2+} at the tetrahedral (A) site, suggests that there is increasing tendency for triangular spin arrangement on the B-site which results in decreased A-B exchange interaction.

The observation of the increase in magnetization pinning with increase in Sm content agrees with the increase in the area under the hyperfine field distribution (superparamagnetic doublet) as observed by Mössbauer spectroscopy. This effect is pronounced for the sample with y = 0.05 (Table III and Fig. 6). The increase in coercivity with Sm^{3+} ion concentration is due to an increased magnetic anisotropy resulting from the pinning of the spins of the Mn^{2+} and Fe^{3+} ions at the Sm^{3+} site. Considering the increase in $\boldsymbol{H_c}$, the decrease in $\boldsymbol{\eta_B}$ and decrease in particle size with increase in Sm^{3+} content suggests that there exists an effective anisotropy due to pinning of the spins which shields the magnetization of the core of the particle from particle-particle interaction which makes the particles more superparamagnetic and the anisotropy appears to be of cubic anisotropy type. Furthermore, as the Mössbauer spectroscopy results depend neither on the particle size nor on the spin glass structure, they suggest the pinning of magnetic moments is due to the magnetic defect created by the presence of Sm^{3+} ions.

The variations of all the parameters ($\boldsymbol{\eta_B}$, $\boldsymbol{H_c}$, $\boldsymbol{S}$ and $\boldsymbol{K}$) with Sm^{3+} content in the samples extracted from the hysteresis loops can be observed from Table IV. In order to realize the presence of magnetic defects due to Sm-doping, we have calculated the magnetic particle sizes by using Eq. 5. They are listed in Table IV and plotted in Fig. 9. To visualize the magnetic

pinning induced in the samples due to Sm-doping, we plotted the magnetic hyperfine field ($\boldsymbol{B_{hf}}$), average crystallite size (<***d***>), magnetic particle size ($\boldsymbol{D_m}$) and spectral area under the sextet distribution observed from Mössbauer spectra, against the Sm-content 'y' (Fig. 9). From the plot, we can observe the decreasing trend of all the parameters with increasing Sm^{3+} concentration up to y = 0.03. Interestingly, although crystallite sizes calculated from XRD results decreased continuously with Sm^{3+} concentration up to y = 0.05, $<D_m>$ and Mössbauer spectral area increased while the $<B_{hf}>$ remains constant for y = 0.05. This suggests that there are two competing effects present in all our samples: (i) paramagnetism due to lower exchange interaction energy; and (ii) magnetization pinning observed as magnetic (defects) anisotropy and enhanced $\boldsymbol{H_c}$. The pinning of the spins at higher Sm^{3+} content is dominant, which increase the magnetic anisotropy as well as $\boldsymbol{H_c}$. This is also the reason for increase in the area under the superparamagnetic part of the Mössbauer spectra (Fig. 6).

4. CONCLUSION

Samarium substituted Mn-Zn ferrites were successfully synthesized by propellant chemistry route using a mixture of fuels (urea and glucose). The effect of Sm^{3+} ion substitution on the structural and magnetic properties of these ferrites was studied at room temperature. The X-ray diffraction revealed that all the samples were mono-phased with cubic spinel structure. The crystallites were in nano-size regime. The average crystallite size decreased with increasing Sm concentration. The position of absorption bands in FTIR spectra confirmed the formation of cubic spinel ferrite. The Sm-substituted Mn-Zn ferrite particles showed enhanced hard ferrimagnetic nature with increasing Sm-content. The value of saturation magnetization was found to decrease, but, the coercivity increased with Sm-content. Also, the magnetic particle size and magneton number were found to decrease gradually with the increase in Sm^{3+} concentration. The paramagnetic-like Sm^{3+} ion substitution in octahedral site reduced the exchange interaction between A and B sites that resulted in decrease of saturation magnetization. Furthermore,

Mössbauer spectroscopy results suggest the existence of local disorder in the arrangement of cations in the sub-lattice of samples. Also, the pinning of magnetic moments was found to be solely due to Sm^{3+} ions with related effects arising from particle size variation. These observations in our sample suggest that the synthesized ferrites can be potentially used in applications involving a wide range of frequencies.

ACKNOWLEDGEMENTS

The authors (JAV and BRS) are thankful to the UGC, New Delhi, for the financial support received through the Major Research project (File No.UGC-MRP-41-946). RK is thankful to CSIR, New Delhi for financial support received through Junior Research Fellowship. The authors would like to express sincere thanks to Prof. A. Sundaresan, Chemistry and Physics of Materials Unit (CPMU), Jawaharlal Nehru Centre for Advanced Scientific Research (JNCASR) for providing magnetization measurement facility. The work at IISc Bangalore was supported by the ISRO-IISc STC project (Code Number-ISTC/CMR/BS/355).

References

[1] P. Hu, H. B. Yang, De-an Pan, H. Wang, J. J. Tian, S. G. Zhang, X. F. Wang, A. A. Volinsky, Heat treatment effects on microstructure and magnetic properties of Mn–Zn ferrite powders, J. Magn. Magn. Mater. 322 (2010) 173-177.

[2] A. C. F. M. Costa, V. J. Silva, C. C. Xin, D. A. Vieira, D. R. Cornejo, R. H. G. A. Kiminami, Effect of urea and glycine fuels on the combustion reaction synthesis of Mn-Zn ferrites: Evaluation of morphology and magnetic properties, J. Alloys Compd. 495 (2010) 503-505.

[3] M. M. Hessien, M. M. Rashad, K. El-Barawy, I. A. Ibrahim, Influence of manganese substitution and annealing temperature on the formation, microstructure and magnetic properties of Mn-Zn ferrites, J. Magn. Magn. Mater. 320 (2008) 1615-1621.

[4] A. Goldman, Modern Ferrite Technology, 2nd ed. Springer, Berlin (2006).

[5] R. N. Panda, J. C. Shih, T. S. Chin , Magnetic properties of nano-crystalline Gd- or Pr-substituted $CoFe_2O_4$ synthesized by the citrate precursor technique, J. Magn. Magn. Mater. 257 (2003) 79-86.

[6] E. Ateia, M. A. Ahmed, A. K. El-Aziz, Effect of rare earth radius and concentration on the structural and transport properties of doped Mn-Zn ferrite, J. Magn. Magn. Mater. 311 (2007) 545-554.

[7] S. Thankachan, B. P. Jacob, S. Xavier, E. M. Mohammed, Effect of samarium substitution on structural and magnetic properties of magnesium ferrite nanoparticles, J. Magn. Magn. Mater. 348 (2013) 140-145.

[8] M. A. Ahmed, N. Okasha, A. A. Mohamed, I. Mmdouh, Optimizing the structure and magnetic properties of SmCo nanoferrites synthesized by auto-combustion processing techniques, J. Magn. Magn. Mater. 358-359 (2014) 32-37.

[9] M. M. Rashad, R. M. Mohamed, H. El-Shall, Magnetic properties of nanocrystalline Sm- substituted $CoFe_2O_4$ synthesized by citrate precursor method, J. Magn. Magn. Mater.198 (2008)139-146.

[10] A. B. Gadkari, T. J. Shinde, P. N. Vasambekar, Structural analysis of Sm^{3+} doped nanocrystalline Mg-Cd ferrites prepared by oxalate co-precipitation method, Mater. Charact. 60 (2009) 1328-1333.

[11] J. Chand, S. Verma, M. Singh, Structural, magnetic and Mössbauer spectral studies of Sm^{3+} ions doped Mg ferrites synthesized by solid state reaction technique, J. Alloys Compd. 552 (2013) 264-268.

[12] E. De Fazio, P. G. Bercoff, S. E. Jacobo, Electromagnetic properties of manganese–zinc ferrite with lithium substitution, J. Magn. Magn. Mater. 323 (2011) 2813-2817.

[13] K. Praveena, S. R. Murthy, Magneto acoustical emission in nanocrystalline Mn-Zn ferrites, Mater. Research Bulletin 48 (2013) 4826-4833.

[14] R. E. Rosensweig, Ferrohydrodynamics, Dover, New York (1997).

[15] L. J. Love, J. F. Jansen, T. E. McKnight, Y. Roh, T. J. Phelps, A magnetocaloric pump for microfluidic applications, IEEE transactions on Nano bioscience 3 (2004) 101-110.

[16] L. Zhuang, W. Zhang, Y. Zhao, D. Li, W. Wu, H. Shen, Temperature sensitive ferrofluid composed of $Mn_{1-x}Zn_xFe_2O_4$ nanoparticles prepared by a modified hydrothermal process, Powder Technology 217 (2012) 46-49.

[17] H. Matsuki, K. Murakami, Performance of an automatic cooling device using a temperature-sensitive magnetic fluid, J. Magn. Magn. Mater. 65 (1987) 363-365.

[18] K. Nakatsuka, Y. Hama, J. Takahashi, Heat transfer in temperature sensitive magnetic fluids, J. Magn. Magn. Mater. 85 (1990) 207-209.

[19] R. V. Upadhyay, R. V. Mehta, K. Parekh, D. Srinivas, R. P. Pant, Gd-substituted ferrite ferrofluid: a possible candidate to enhance pyromagnetic coefficient, J. Magn. Magn. Mater. 201 (1999) 129-132.

[20] S. H. Chen, S. C. Chang, I. N. Lin, "The influence of grain boundary internal stress on permeability: temperature curve for Mn-Zn ferrites", J. Magn. Magn. Mater. 209 (2000) 193-196.

[21] R. Arulmurugan, B. Jeyadevan, G. Vaidyanathan, S. Sendhilnathan, Effect of zinc substitution on Co-Zn and Mn-Zn ferrite nanoparticles prepared by co-precipitation, J. Magn. Magn. Mater. 288 (2005) 470-477.

[22] C. Venkataraju, G. Sathishkumar, K. Sivakumar, Effect of cation distribution on the structural and magnetic properties of nickel substituted nanosized Mn-Zn ferrites prepared by co-precipitation method, J. Magn. Magn. Mater. 322 (2010) 230-233.

[23] R. Arulmurugan, G. Vaidyanathan, S. Sendhilnathan, B. Jeyadevan, Mn-Zn ferrite nanoparticles for ferrofluid preparation: Study on thermal–magnetic properties, J. Magn. Magn. Mater. 298 (2006) 83-94.

[24] M. Rozman, M. Drofenik, Hydrothermal synthesis of manganese zinc ferrites, J. Am. Ceram. Soc. 78 (1995) 2449-2455.

[25] D. Makovec, M. Drofenik, A. Znidarsic, Hydrothermal synthesis of manganese zinc Ferrite powders from oxides, J. Am. Ceram. Soc. 82 (1999) 1113-1120.

[26] K. Winiarska, I. Szczygiel, R. Klimkiewicz, Manganese-zinc ferrite synthesis by the sol-gel autocombustion method. Effect of the Precursor on the Ferrite's Catalytic Properties, Ind. Eng. Chem. Res. 52 (2013) 353-361.

[27] J. Azadmanjiri, Preparation of Mn-Zn ferrite nanoparticles from chemical sol-gel combustion method and the magnetic properties after sintering, J. Non. Cryst. Solids. 353 (2007) 4170-4173.

[28] C. H. Chen, M. H. J. Emond, E. M. Kelder, B. Meester, J. Schoonman, Electrostatic sol-spray deposition of nanostructured ceramic thin films, J. Aerosol Sci. 30 (7) (1999) 959-967.

[29] A. Thakur, M. Singh, Preparation and characterization of nanosize $Mn_{0.4}Zn_{0.6}$ Fe_2O_4 ferrite by citrate precursor method, Ceram. Inter. 29 (2003) 505-511.

[30] A. C. F. M. Costa, V. J. Silva, D. R. Cornejo, M. R. Morelli, R. H. G. A. Kiminami, L. Gama, Magnetic and structural properties of $NiFe_2O_4$ ferrite nanopowder doped with Zn^{2+}, J. Magn. Magn. Mater. 320 (2008) e370–e372.

[31] K. C. Patil, M. S. Hegde, Tanu Rattan, S. T. Aruna, Chemistry of Nanocrystalline Oxide Materials, Combustion Synthesis, Properties and Applications, World Scientific Publishing Co. Pte. Ltd., Singapore (2008).

[32] S. Sam, A. S. Nesaraj, Preparation of $MnFe_2O_4$ Nanoceramic Particles by Soft Chemical Routes, Intl. J. Appl. Sci. Eng. 9 (4) (2011) 223-239.

[33] J. Rodriguez-Carvajal, FULLPROF: A Program for Rietveld Refinement and Pattern Matching Analysis, Abstracts of the Satellite Meeting on Powder Diffraction of the XV Congress of the IUCr, p. 127, Toulouse, France (1990).

[34] R. A. Young, The Rietveld method, IUCr, 5, 1-39, Oxford University Press, Oxford (1993).

[35] G. K. Williamson, W. H. Hall, X-ray line broadening from filed Aluminium and Wolfram, Acta Metall. 1 (1953) 22–31.

[36] R. A. Brand, Improving the validity of hyperfine field distributions from magnetic alloys : Part I: Unpolarized source, Nucl. Instrum. Methods B 28 (1987) 398-416.

[37] R. A. Brand, Improving the validity of hyperfine field distributions from magnetic alloys: Part II: Polarized source and spin texture, Nucl. Instrum. Methods B 28 (1987) 417-432.

[38] M. Ishii, M. Nakahira, T. Yamanka, Infrared absorption spectra and cation distributions in $(Mn, Fe)_3O_4$, J. Solid State Commun. 11 (1972) 209-212.

[39] E. C. Stoner, E. P. Wohlfarth, A Mechanism of Magnetic Hysteresis in Heterogeneous Alloys, Philos. Trans. R. Soc. London A 240 (826) (1948) 599–642.

[40] S. Giri, S. Samanta, S. Maji, S. Ganguli, A. Bhumik, Magnetic properties of α-Fe_2O_3 nanoparticle synthesized by a new hydrothermal method, J. Magn. Magn. Mater. 285 (2005) 296-302.

[41] R. Topkaya, A. Baykal, A. Demir, Yafet–Kittel-type magnetic order in Zn-substituted cobalt ferrite nanoparticles with uniaxial anisotropy, J. Nanopart. Res. 15:1359 (2013) 1-18.

[42] J. Smit, H. P. J. Wijn, Ferrites, p. 158, J. Wiley and Sons, New York (1959).

[43] K. Parekh, R.V. Upadhyay, L. Belova, K. V. Rao., Ternary monodispersed $Mn_{0.5}Zn_{0.5}Fe_2O_4$ ferrite nanoparticles: preparation and magnetic characterization, Nanotechnology 17 (2006) 5970-5975.

[44] N. Kikukawa, M. Sugasawa, S. Kobayashi, Preparation of Spinel-Type Ferrite Fine Particles via Plasma Route Using Amorphous Citrate Gel as a Precursor, Jpn. J. Appl. Phys. 41 (2002) 5991-5992.

[45] J. M. Hastings, L. M. Corliss, Neutron Diffraction Studies of Zinc Ferrite and Nickel Ferrite, Rev. Mod. Phys. 25 (1) (1953) 114-119.

[46] C. Upadhyay, H. C. Verma, Cation distribution in nanosized Ni–Zn ferrites, J. Appl. Phys. 95 (2004) 5746-5751.

[47] A. Miller, Distribution of Cations in Spinels, J. Appl. Phys. 30 (1959) 24S-25S.

[48] M. H. Mahmoud, H. H. Hamdeh, J. C. Ho, M. J. O'Shea, J. C. Walker, Mössbauer studies of manganese ferrite fine particles processed by ball-milling, J. Magn. Magn. Mater. 220 (2000) 139-146.

[49] R. D. Shannon, Revised effective ionic radii and systematic studies of interatomic distances in halides and chalcogenides, Acta Cryst. A32 (1976) 751-767.

[50] Electronic Table of Shannon Ionic Radii, J. David Van Horn (2001), downloaded MO/DA/YEAR (04/14/2015). http://v.web.umkc.edu/vanhornj/shannonradii.htm

[51] S. A. Oliver, H. H. Hamdeh, J. C. Ho, Localized spin canting in partially inverted $ZnFe_2O_4$ fine powders, Phys. Rev. B 60 (1999) 3400-3405.

[52] H. H. Hamdeh, J. C. Ho, S. A. Oliver, R. J. Willey, G. Oliveri, G. Busca, Magnetic properties of partially-inverted zinc ferrite aerogel powders, J. Appl. Phys. 81 (1997) 1851-1857.

[53] L. Ai, J. Jiang, H. Gao, Effect of samarium doping on the structural and Magnetic properties of the lithium nickel ferrite, Mod. Phys. Letters B 22 (21) (2008) 2027-2033.

[54] O. M. Hemeda, IR spectral studies of $Co_{0.6}Zn_{0.4}Mn_xFe_{2-x}O_4$ ferrites, J. Magn. Magn. Mater. 281 (2004) 36-41.

[55] V. A. Potakova, N. D. Zverev, V. P. Romanov, On the Cation Distribution in $Ni_{1-x-y}Fe_x^{2+}Zn_yFe_2^{3+}0_4$, Spinel Ferrites, Phys. Stat. Sol. (a) 13 (1972) 623-627.

[56] E. Melagiriyappa, H. S. Jayanna., Structural and magnetic susceptibility studies of samarium substituted magnesium-zinc ferrites, J. Alloys Compd. 482 (2009) 147-150.

[57] B. N. Figgis, in: Comprehensive Coordination Chemistry, G. Wilkinson, Gillard, J. A. McCleverty (Eds.), 1, Pergamon, New York, p. 261 (1987).

[58] K. J. Standley, Oxide Magnetic Materials, Clarendon Press, Oxford, p. 52 (1972).

[59] L. Néel, Antiferromagnetism and Ferrimagnetism, Proce. Phy. Soc. London, 65, 11 395A (1952) 869-885.

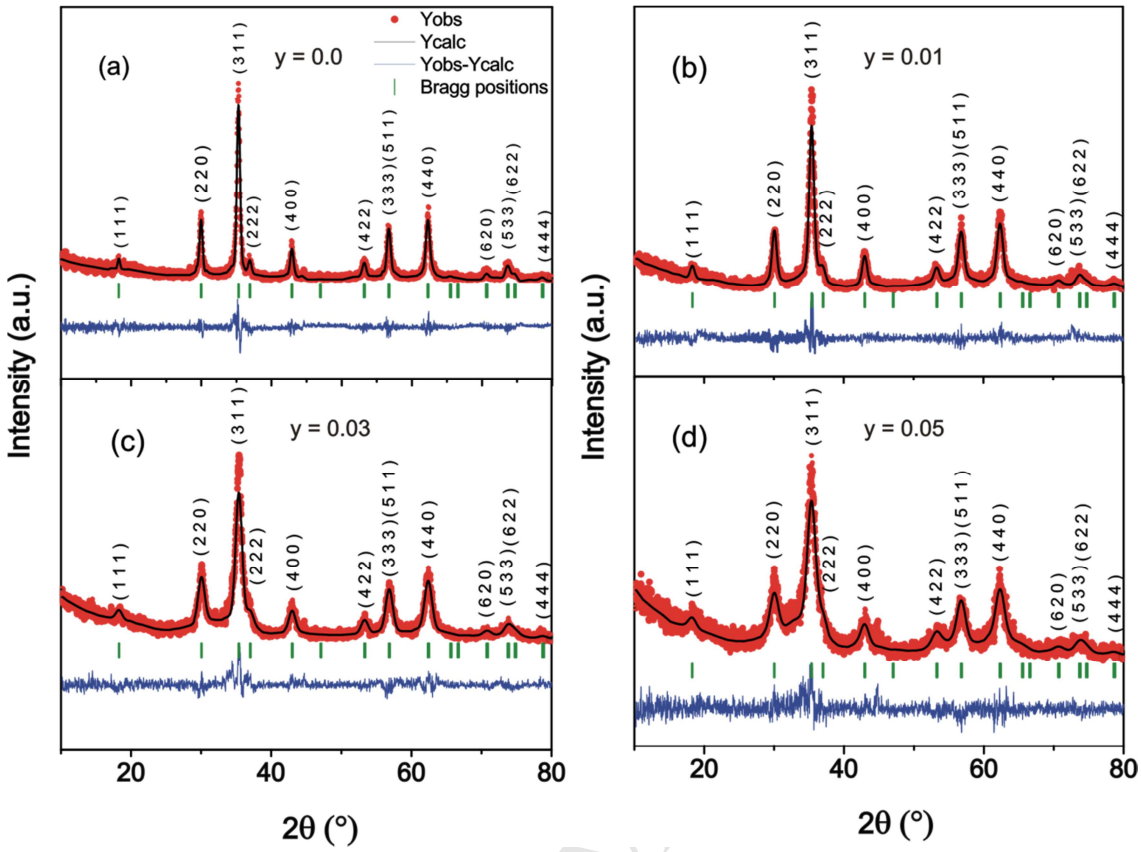

FIG. 1. Rietveld refined XRD patterns for $Mn_{0.5}Zn_{0.5}Fe_{2-y}O_4$ samples, y = 0.0 (a), 0.01 (b), 0.03 (c) and 0.05 (d). All major reflections are indexed.

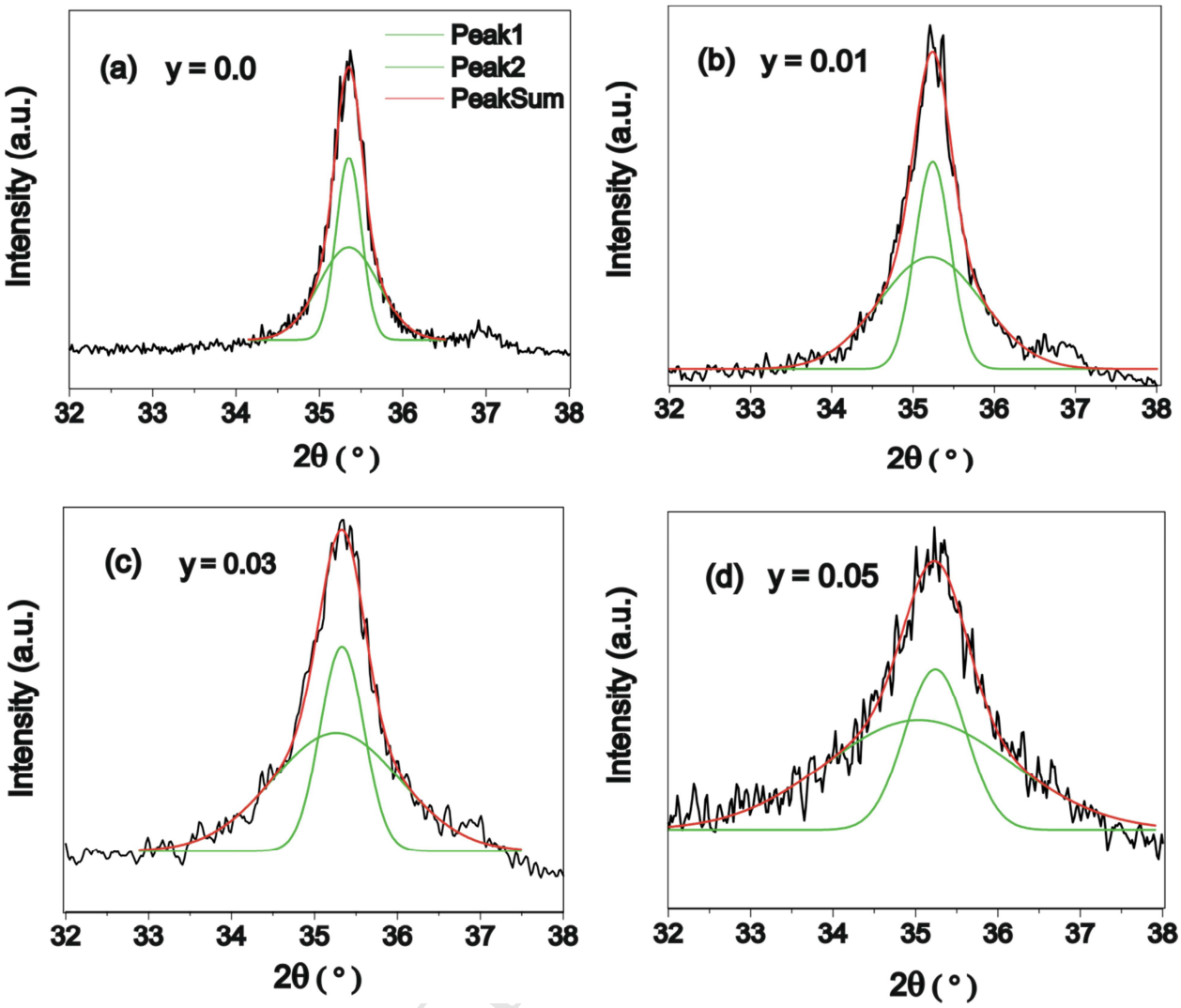

FIG. 2. Pseudo-Voigt fits to the (311) peak of $Mn_{0.5}Zn_{0.5}Fe_{2-y}Sm_yO_4$ samples with y = 0.0 (a), 0.01 (b), 0.03 (c) and 0.05 (d).

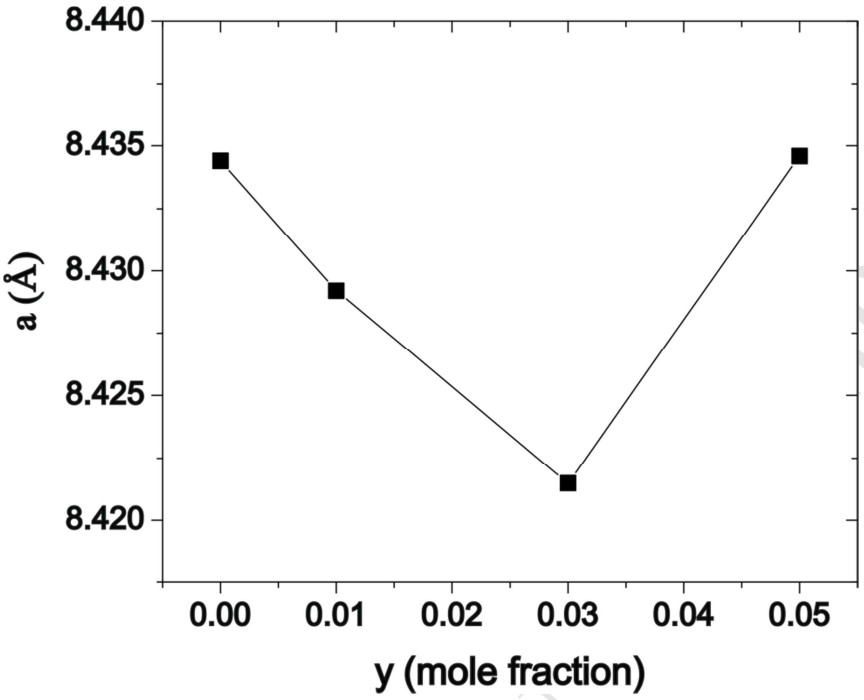

FIG.3. Variation of lattice parameter (**a**) with Sm^{3+} content (y) in $Mn_{0.5}Zn_{0.5}Sm_yFe_{2-y}O_4$ samples.

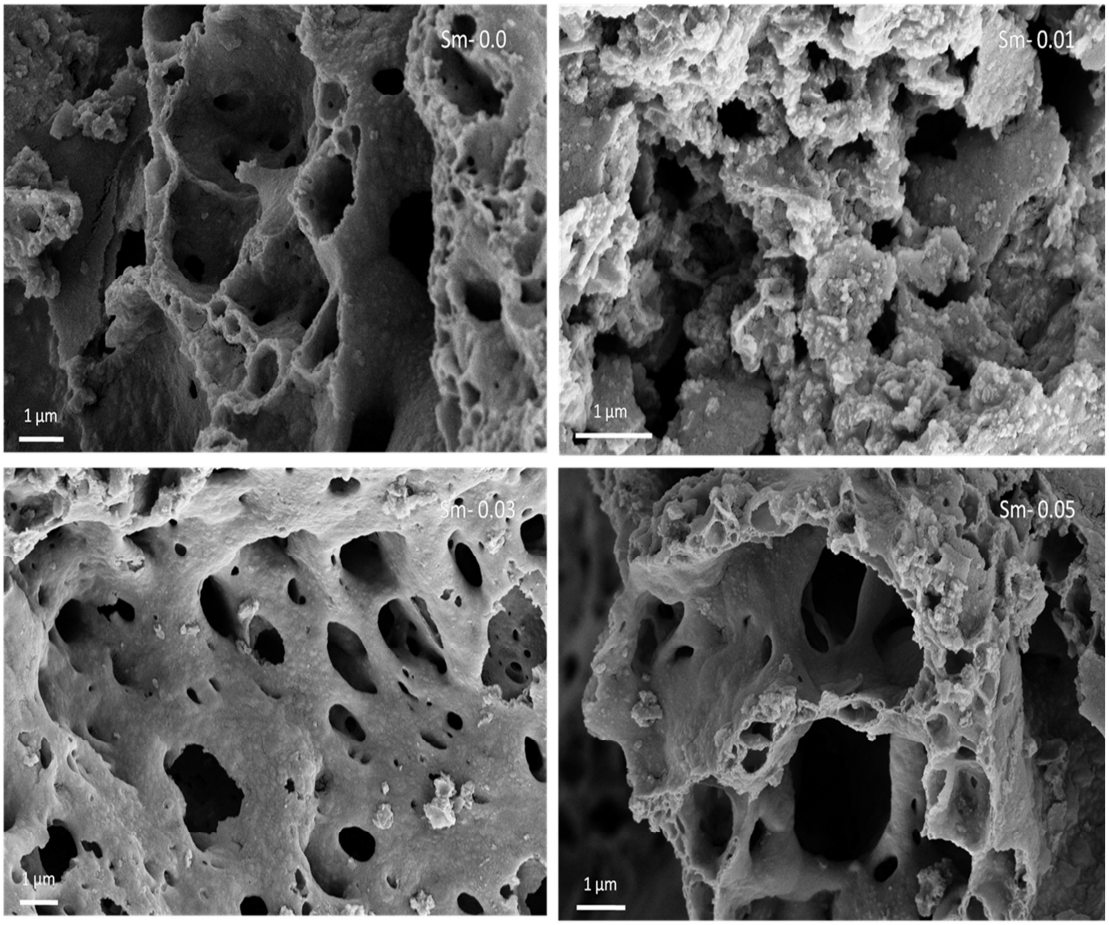

FIG. 4. SEM images for $Mn_{0.5}Zn_{0.5}Fe_{2-y}O_4$ samples, y = 0.0 (a), 0.01 (b), 0.03 (c) and 0.05 (d).

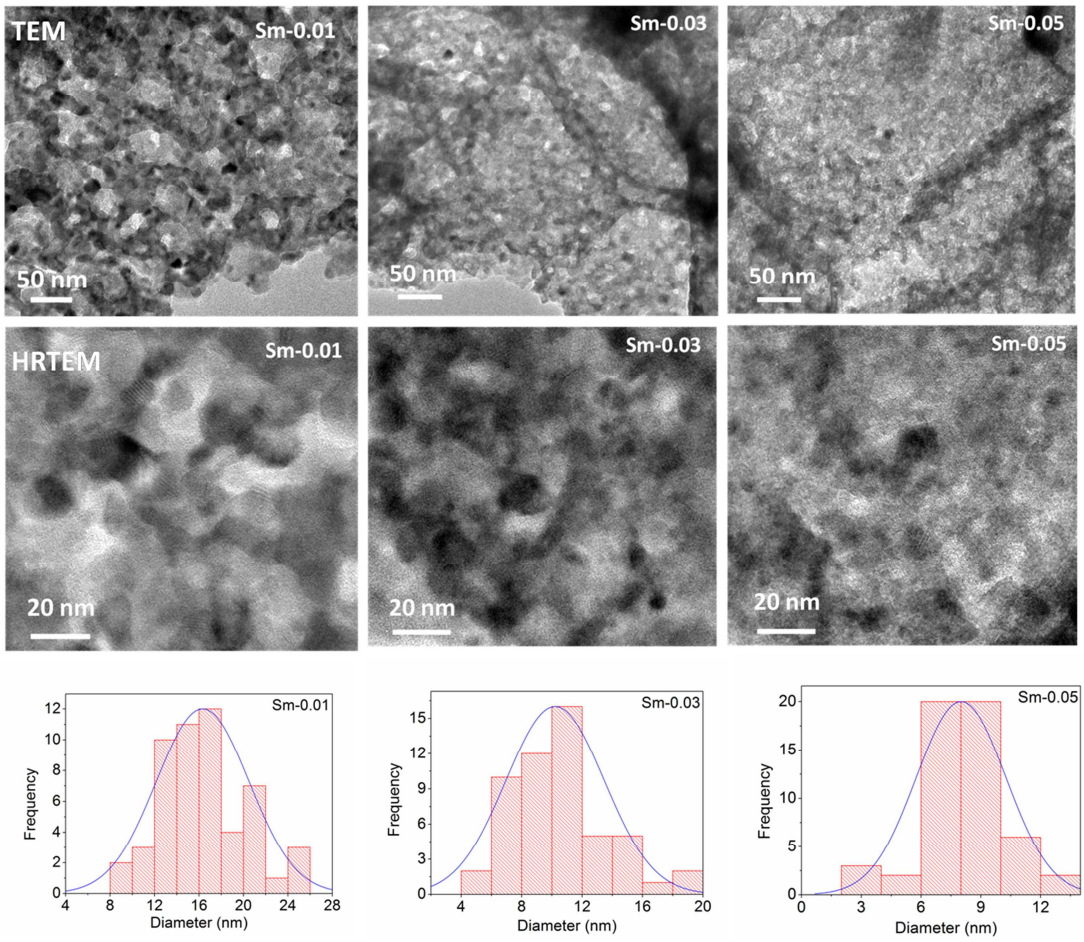

(a) \(b) (c)

FIG. 5. TEM, HRTEM images and particle size distribution for $Mn_{0.5}Zn_{0.5}Fe_{2-y}O_4$ samples, y = 0.01 (a), 0.03 (b), and 0.05 (c).

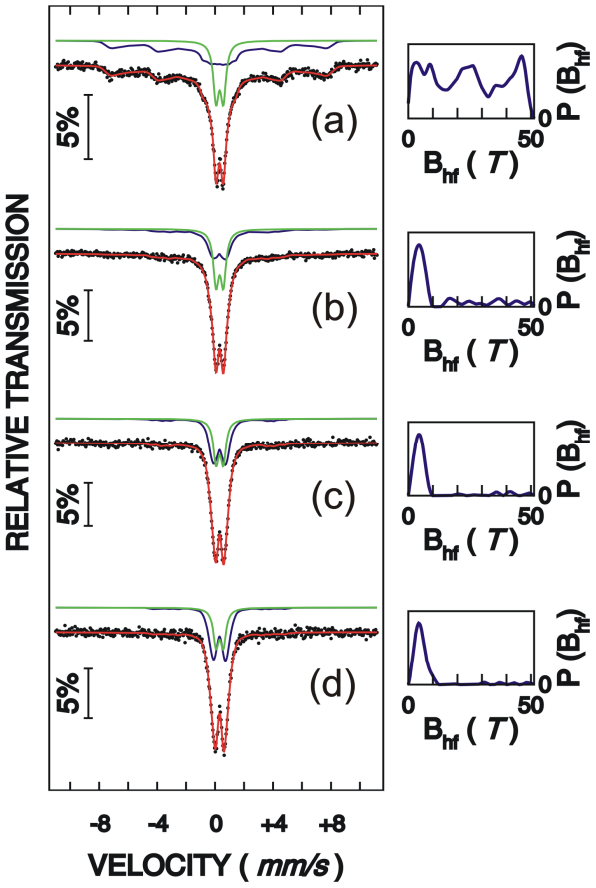

FIG. 6. Least square fit Mössbauer spectra of $Mn_{0.5}Zn_{0.5}Fe_{2-y}Sm_yO_4$ samples: (a) y = 0.0, (b) y = 0.01, (c) y = 0.03 and (d) y = 0.05, measured at RT. On the right hand side of each spectrum, the distribution profiles of magnetic hyperfine field ***P(B$_{hf}$)*** are shown.

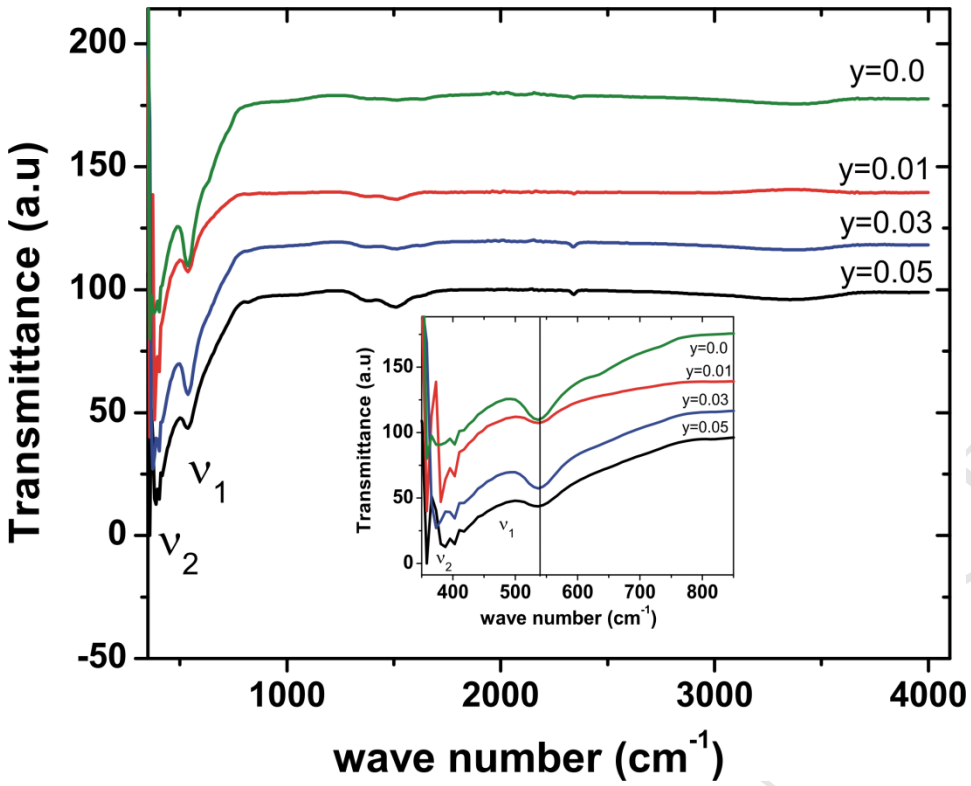

FIG.7. FTIR spectra of $Mn_{0.5}Zn_{0.5}Sm_yFe_{2-y}O_4$ samples with y = 0.0, 0.01, 0.03 and 0.05.The inset shows the zoomed in view of the two band positions (tetrahedral: ~540 cm^{-1} and Octahedral: ~ 390 cm^{-1}).

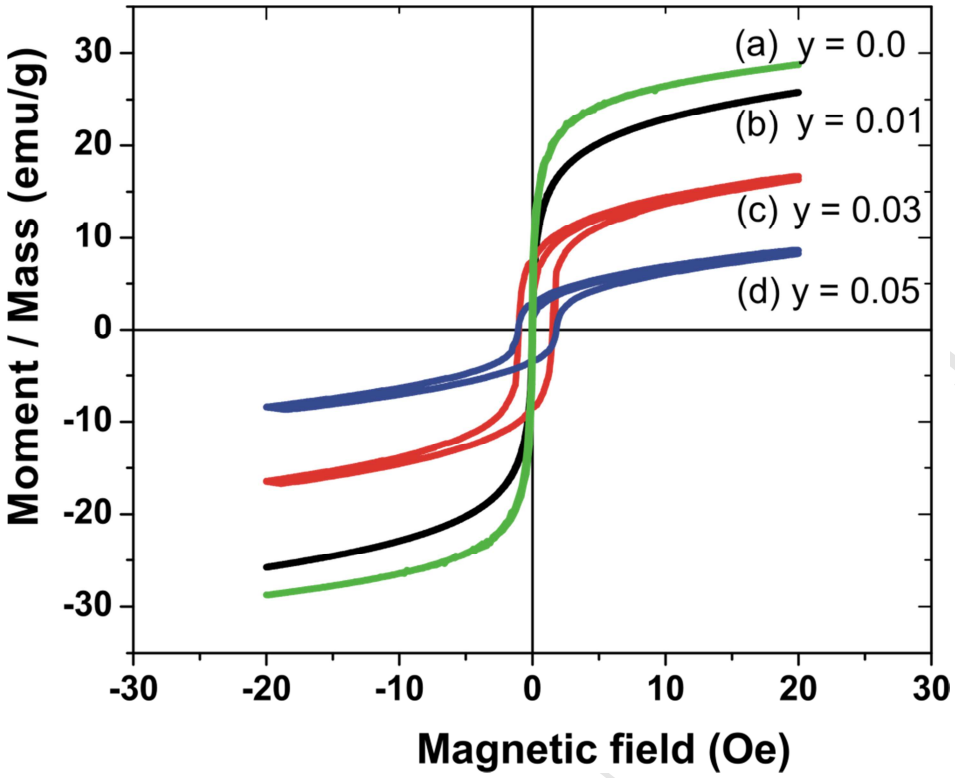

FIG.8. Magnetic hysteresis loops for $Mn_{0.5}Zn_{0.5}Sm_yFe_{2-y}O_4$ samples with y = 0.0 (a), 0.01 (b), 0.03 (c) and 0.05 (d).

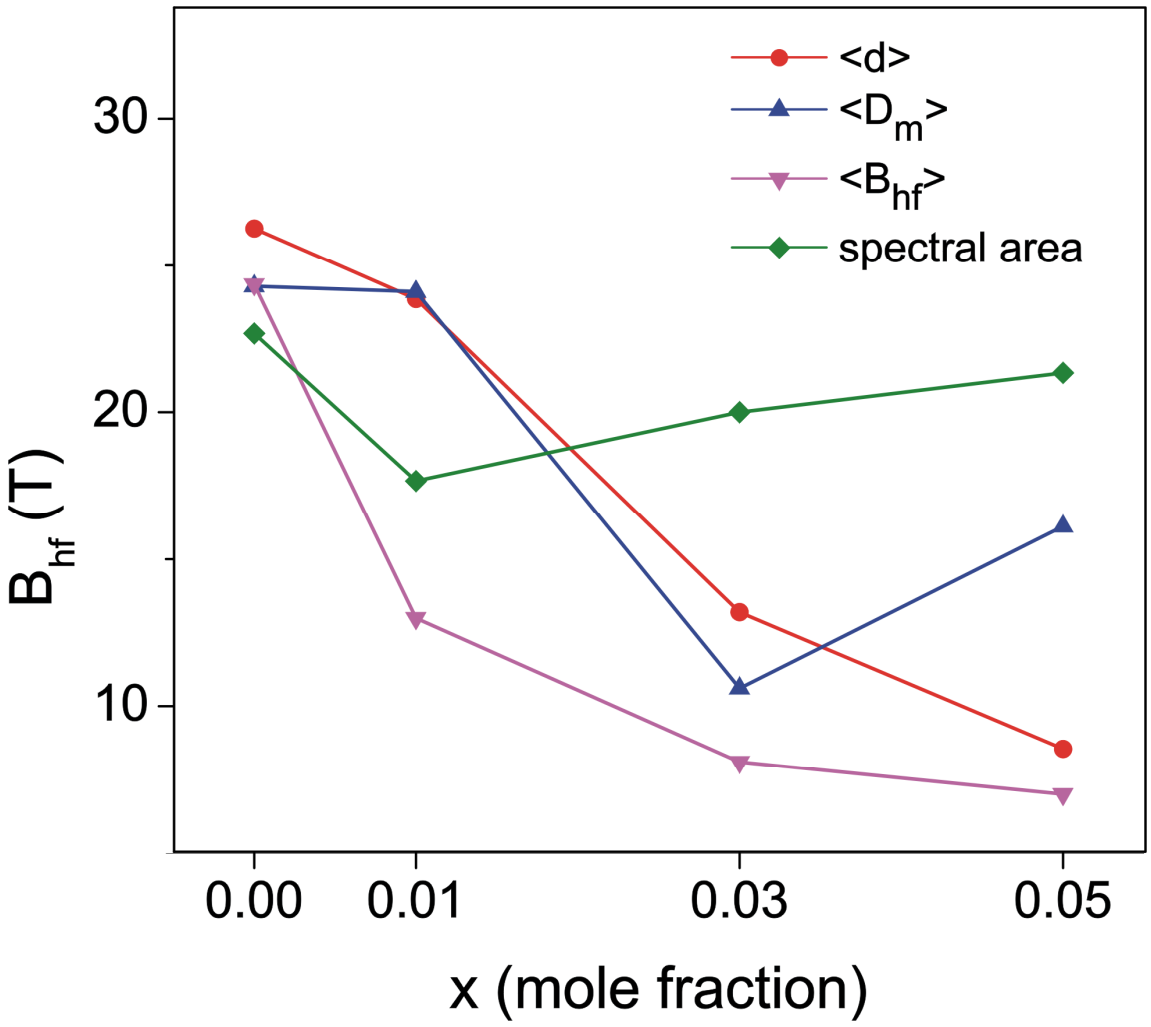

FIG. 9. Variation of selected structural and magnetic parameters of the $Mn_{0.5}Zn_{0.5}Fe_{2-y}Sm_yO_4$ samples with 'y'. In the plot, the variation in magnetic hyperfine field ($\boldsymbol{B_{hf}}$), average crystallite size (<***d***>), magnetic particle size ($\boldsymbol{D_m}$) and crystalline spectral area show a similar trend with theSm-content 'y'. The Y-scale in the plot corresponds to the actual measured value of <$\boldsymbol{B_{hf}}$>, whereas the Y-scales corresponding to $\boldsymbol{D_m}$ values (in nm) are enhanced by a factor of 3, <***d***> values (in nm) are enhanced by a factor of 1.5 and the spectral area values (in %) are reduced by a factor of 3 for the purpose of comparison in the same plot.

Table I. Structural parameters of $Mn_{0.5}Zn_{0.5}Fe_{2-y}Sm_yO_4$ samples, obtained from Rietveld refinement of XRD data. The values within the brackets represent the minimum and maximum crystallite sizes. "***a***" is the lattice parameter. The particle sizes obtained from the TEM analysis are given in the last column.

y	"***a***" (Å)	Theoretical density (g/cc)	X-ray density (g/cc)	Reliability factors				Average crystallite size	
				R_{wp}	R_p	$R_{ex\backslash p}$	χ^2	$\langle d_{XRD} \rangle$ (nm)	$\langle d_{TEM} \rangle$ (nm)
0.00	8.4344	5.595	5.425	40	35	34	1.0	16 [9-23]	-
0.01	8.4292	5.615	5.503	47	40	49	0.7	11 [5-16]	16 ± 4
0.03	8.4215	5.648	5.643	46	39	51	0.6	8 [3-12]	10 ± 3
0.05	8.4346	5.683	5.753	50	50	43	1.1	6 [3-11]	8 ± 2

Table II. The cation occupancies at tetrahedral (A) and octahedral (B) sites of $Mn_{0.5}Zn_{0.5}Fe_{2-y}Sm_yO_4$ samples per formula cell, obtained from the Rietveld refinement of XRD data.

y	Cation occupancy mole fraction and (in %)								Sub-lattice magnetic moment	
	Zn^{2+}		Mn^{2+}		Fe^{3+}		Sm^{3+}			
	A	B	A	B	A	B	A	B	M_A	M_B
0.00	0.5 (100)	0.0	0.426 (85.2)	0.074 (14.8)	0.074 (3.70)	1.926 (96.30)	0.0	0.0	1.225	9.775
0.01	0.5 (100)	0.0	0.419 (83.8)	0.081 (16.2)	0.081 (4.05)	1.909 (95.95)	0.0	0.001 (100)	1.243	9.708
0.03	0.5 (100)	0.0	0.411 (82.2)	0.089 (17.8)	0.089 (4.45)	1.881 (95.55)	0.0	0.003 (100)	1.267	9.588
0.05	0.5 (100)	0.0	0.401 (80.2)	0.099 (19.8)	0.099 (4.95)	1.851 (95.05)	0.0	0.005 (100)	1.267	9.460

Table III. Mössbauer spectral parameters obtained after the least square fitting of the Mössbauer spectra (Fig. 2) of $Mn_{0.5}Zn_{0.5}Fe_{2-y}Sm_yO_4$ samples. Average values of Isomer shift (<***IS***>) and magnetic hyperfine field (<$\boldsymbol{B_{hf}}$>), quadrupole splitting (***QS***), relative spectral area and spectral line width (FWHM) are listed. Sub-spectra designated by S and D abbreviate for sextet distributions and doublet, respectively. The values of ***IS*** are given with respect to the ^{57}Co-source (Rh-matrix).

y (mole fraction)	Sub-spectrum	<***IS***> (mm/s)	***QS*** (mm/s)	<$\boldsymbol{B_{hf}}$> (T) (± 0.5 T)	Peak values at $\boldsymbol{P(B_{hf})}$	Spectral area (%)
0.00	S11	0.204	-0.023	24.34	3.6, 9, 25, 46	68
	D11	0.235	0.500			32
0.01	S21	0.195	0.008	13	4.5, 17, 37	53
	D21	0.235	0.500			47
0.03	D31	0.226	-0.039	8.1	4.5	60
	D32	0.235	0.500			40
0.05	D41	0.187	-0.064	7	4.5	64
	D42	0.235	0.500			36

Table IV. The magnetic parameters obtained from the M-H loops for $Mn_{0.5}Zn_{0.5}Fe_{2-y}Sm_yO_4$ samples. Saturation magnetization ($\boldsymbol{M_S}$), remanence ($\boldsymbol{M_r}$), reduced remanence ***S*** (= $\boldsymbol{M_r/M_s}$), coercivity ($\boldsymbol{H_c}$), magneton number ($\boldsymbol{\eta_B}$), anisotropy constant (***K***), Y-K angle ($\boldsymbol{\alpha_{Y\text{-}K}}$), initial susceptibility ($\boldsymbol{\chi_i}$) and upper limit of the magnetic particle size ($\boldsymbol{D_m}$) for the samples are listed against Sm^{3+} concentration (y).

y	$\boldsymbol{M_s}$ (emu/g)	$\boldsymbol{M_r}$ (emu/g)	***S***	$\boldsymbol{H_c}$ (Oe)	***K*** (erg/Oe)	$\boldsymbol{\eta_B}$ ($\boldsymbol{\mu_B}$)	$\boldsymbol{\alpha_{Y\text{-}K}}$ (°)	$\boldsymbol{\chi_i}$	$\boldsymbol{D_m}$ (nm) X-ray	$\boldsymbol{D_m}$ (nm) Theoretical
0.00	24.6	3.01	0.122	68	1698	1.0387	76.61	0.07	7.9	7.9
0.01	20.7	0.66	0.033	21	441	0.8775	77.38	0.0404	7.5	7.4
0.03	12.4	8.09	0.655	1258	24275	0.5277	79.21	0.0017	3.6	3.6
0.05	4.8	3.26	0.676	1453	10947	0.2076	81.04	8.9E-4	5.4	5.4

Highlights

1. Sm^{3+} substituted MnZn-ferrite samples were prepared by propellant chemistry route.
2. Particle sizes and M_s values decrease with increasing Sm^{3+} concentration.
3. Lattice parameter decreases with Sm^{3+} conc. despite Sm^{3+} having bigger size.
4. Magnetic defects created by Sm^{3+} ions enhance the magnetic pinning.
5. The effective magnetic particle size increases by increasing Sm^{3+}- doping.